Three-color single-molecule imaging reveals conformational dynamics of dynein undergoing motility

Stefan Niekamp[a,b], Nico Stuurman[a,b], Nan Zhang[a,b], and Ronald D. Vale[a,b,1,2]

[a]HHMI, University of California, San Francisco, CA 94158; and [b]Department of Cellular and Molecular Pharmacology, University of California, San Francisco, CA 94158

The motor protein dynein undergoes coordinated conformational changes of its domains during motility along microtubules. Previous single-molecule studies analyzed the motion of the AAA rings of the dynein homodimer, but not the distal microtubule-binding domains (MTBDs) that step along the track. Here, we simultaneously tracked with nanometer precision two MTBDs and one AAA ring of a single dynein as it underwent hundreds of steps using three-color imaging. We show that the AAA ring and the MTBDs do not always step simultaneously and can take differently sized steps. This variability in the movement between the AAA ring and MTBDs results in an unexpectedly large number of conformational states of dynein during motility. Extracting data on conformational transition biases, we could accurately model dynein stepping in silico. Our results reveal that the flexibility between major dynein domains is critical for dynein motility.

dynein | motor proteins | single molecule | fluorescence microscopy

The microtubule-based motor protein dynein belongs to the AAA+ (ATPases Associated with diverse cellular Activities) family of motors and is responsible for the majority of minus-end-directed motility along microtubules (1, 2). Dyneins play key roles in many cellular processes and maintaining cellular architecture, including cargo transport, cilia motility, and the construction of the mitotic spindle (3–6). Mutations or defects in cytoplasmic dynein are linked to several pathologies including cancers and neurological diseases (7, 8).

Compared to kinesin (9, 10) and myosin (11, 12), cytoskeletal motors that have compact, globular motor domains, dynein is much larger and more complex with a size of ∼1.4 MDa. Dynein is composed of two heavy chains and several associated polypeptide chains. The associated chains primarily bind to the N-terminal tail region to dimerize the heavy chains, regulate dynein's function, and attach the motor to cargo (4, 13, 14). The remaining two-thirds of the heavy chain constitute the motor domain, which is the driver of dynein motility (15). The motor domain itself is divided into several domains: linker, AAA ring, stalk, and microtubule-binding domain (MTBD). The AAA ring consists of six different AAA domains that are linked together as an asymmetric hexameric ring (AAA1 to AAA6), of which only AAA1 to 4 can bind adenosine 5′-triphosphate (ATP) (16–19). On top of the AAA ring lies the N-terminal linker that serves as a mechanical element and connects the motor domain to the N-terminal tail. The large catalytic AAA ring of dynein is separated from the small MTBD by a ∼15-nm-long coiled-coil extending from AAA4 called the stalk (20–22).

Upon ATP binding to AAA1, the motor domain releases from the microtubule and the linker undergoes the priming stroke (bending of the linker). During the priming stroke, the AAA ring has been observed to rotate relative to the linker and therewith bias the rebinding of the MTBD toward the microtubule minus end (1, 23). After ATP hydrolysis, the free MTBD rebinds to the microtubule while the linker undergoes the force-generating power stroke by straightening back to its initial conformation, pulling the cargo with it (1, 24–27). Finally, with adenosine 5′-diphosphate (ADP) release, the mechanochemical cycle can restart.

Initial dynein stepping experiments with a single fluorescent probe revealed that dynein, unlike kinesin, takes side- and backward steps (15). In addition, dynein was shown to take variable step sizes, compared to kinesin, which only takes 8-nm steps (15, 28). Two-color single-molecule experiments revealed that the two AAA rings of dynein move in an uncoordinated manner, allowing one AAA ring to sometimes take multiple steps without any step of the other AAA ring (29, 30). In addition to the well-known hand-over-hand stepping of kinesin and myosin (28, 31), dynein can also move in an inch-worm fashion in which the leading AAA ring can step forward without movement of the trailing AAA ring, or in which the trailing AAA ring can step forward without passing the leading AAA ring (29, 30). Moreover, one active motor domain and an additional microtubule anchor are sufficient to achieve processive and directed motility (32).

Prior single-molecule experiments followed the AAA ring, but not the MTBD that is actually stepping along the microtubule track. Since the AAA ring and the MTBD are separated by the ∼15-nm stalk, which can adopt different angles with respect to the MTBD (2, 33, 34), the position and stepping of the AAA ring may not reflect that of the MTBD. Thus, to have an accurate understanding of dynein stepping, it is important to directly measure the position of the MTBDs relative to the microtubule track and to measure the position of the MTBDs relative to the AAA rings.

Significance

Dynein, a dimeric motor protein, moves along microtubules through adenosine 5′-triphosphate- and thermal-driven motions of two large ring domains (AAA rings) and small microtubule-binding domains (MTBDs) separated by a long coiled-coil. Previous single-molecule studies have tracked the positions of the AAA rings during motility, but not the MTBDs. Here, we tracked the relative positions of both MTBDs and one AAA ring by three-color, nanometer-resolution imaging. The observation of both MTBDs provided a direct measurement of how dynein steps on the tubulin subunits, and the simultaneous observation of three fiducial markers revealed extraordinary flexibility and previously unknown conformational states of the motor during motility. The techniques presented here can be used to explore conformational dynamics of many other macromolecular complexes.

BIOPHYSICS AND COMPUTATIONAL BIOLOGY

Here, we developed a three-color single-molecule microscopy assay that allows simultaneous tracking of the movement of one AAA ring and two MTBDs. In addition to extending existing nanometer accuracy distance measurement and image registration, we also utilized ~6-nm small fluorescent probes (DNA FluoroCubes) that are ~50-fold more photostable than organic dyes (35), allowing many dynein steps to be measured without photobleaching. Using these technical advances, we show that the AAA ring and MTBD sometimes step at different times and take differently sized steps, which gives rise to a large variety of conformations that dynein can adopt as it walks along the track. The transition probabilities between conformations derived from our data are sufficient to recapitulate directed dynein motility using Monte Carlo simulations. Taken together, we conclude that dynein can adopt many conformations, including some previously undescribed ones, and that the AAA ring and MTBD exhibit different stepping behaviors.

Results

Development of a Three-Color Dynein Imaging System. To determine how the AAA ring and MTBD move relative to each other while dynein is stepping along microtubules, we tracked the stepping of a three-color-labeled dynein in which one AAA ring and two MTBDs were labeled with three differently colored fluorophores (Fig. 1*A*). To allow accurate tracking of all three colors with respect to one another with 1-nm resolution, we extended our previously developed two-color image registration routine (36) to three colors (*SI Appendix*, Fig. S1 *A–D*). To validate this approach, we imaged three differently colored dyes placed at well-defined distances on a DNA-origami nanoruler (37, 38) and found that the expected distances among the three dyes were recovered with 1-nm accuracy (*SI Appendix*, Fig. S1 *E–G*).

To create a three-color-labeled dynein dimer in which one AAA ring and two MTBDs are fluorescently labeled, we used the well-studied, truncated yeast cytoplasmic dynein (15) and added an N-terminal SNAP-tag (39), a C-terminal HALO-tag (40), and an internal YBBR-tag (41). In this design, the HALO-tag is positioned on top of the AAA ring and the YBBR-tag is placed in a flexible loop of the MTBD (Fig. 1*B*), enabling us to label both the AAA ring and the MTBD on the same motor domain. For one monomeric motor domain, we labeled the HALO-tag with a six-dye ATTO 488 FluoroCube (35) and the YBBR-tagged MTBD with a six-dye ATTO 674N FluoroCube. For another monomeric motor domain, we only labeled the YBBR-tagged MTBD with a six-dye Cy3N FluoroCube (Fig. 1*A*). To join the two-labeled monomers together into a dimer, we separately labeled the N-terminal SNAP-tag on the monomeric motor domains with reverse-complementary single-stranded DNAs. When combined, the hybridization of the single-stranded DNAs created a dimeric motor as previously described (29). This three-color FluoroCube labeled dynein had a velocity and processivity similar to a green fluorescent protein (GFP)-tagged wild-type dynein (*SI Appendix*, Fig. S2 *A–C* and Movie S1), suggesting that our modifications, including tagging and FluoroCube labeling, did not perturb dynein function.

When we compared a three-color dynein labeled with conventional organic dyes to a dynein labeled with FluoroCubes we found that 4% of the conventional dye-labeled dynein had a signal in all three channels after 50 frames while 75% of FluoroCube-labeled dyneins emitted signals in all three channels (*SI Appendix*, Fig. S2 *F* and *G*). Moreover, the FluoroCube-labeled dynein yielded more precise localizations compared to conventional dyes for the same exposure time of 110 ms (2.4 nm for a Cy3N FluoroCube compared to 7.2 nm for a single conventional dye of the same color; *SI Appendix*, Fig. S2 *D* and *E*). In summary, without using FluoroCubes the tracking of all three domains simultaneously with high resolution would not have been feasible.

Step-Size Analysis of a Three-Color Dynein. We tracked the stepping of three-color-labeled dyneins at low ATP concentration (3 μM) along microtubules to resolve individual steps of all three domains at high spatiotemporal resolution (Fig. 1 *C–E* and Movie S2). For all detected steps analyzed in this study, we found an SD of 3.7 nm for the green-labeled AAA ring, 3.7 nm for the blue-labeled MTBD, and 3.5 nm for the red-labeled MTBD (*SI Appendix*, *Supplementary Note 1*). To enable a fast acquisition of 330 ms with minimal dead time, we optimized the acquisition sequence (see *Materials and Methods* and *SI Appendix*, Fig. S3). Based on dwell-time distributions (*SI Appendix*, Fig. S4*B*), we estimate that this acquisition sequence enabled us to detect more than 95% of all steps of both MTBDs and ~81% of all steps of the green-labeled AAA ring (*SI Appendix*, *Supplementary Note 1*). Together, we resolved 4,500 steps from 54 dynein molecules moving along microtubules (Fig. 1 *D* and *E*).

Using this dataset, we found a similar average step size and percentage of forward steps for the AAA ring when compared to previous studies (29, 30) (Fig. 2 *A* and *B* and *SI Appendix*, Fig. S4). In addition, we were able to analyze the stepping behavior of the MTBDs (Fig. 2*B*). We observed that the MTBDs tend not to pass each other, resulting in inch-worm stepping behavior (*SI Appendix*, Fig. S4), as previously described for the two-color-labeled AAA rings (29, 30). Also in agreement with previous studies of AAA rings (29, 30), we found that with increasing inter-MTBD distance along the on-axis the trailing MTBD was more likely to take the next step compared to the leading MTBD (e.g., at an inter-MTBD on-axis distance of 16 to 24 nm the next step was by the trailing MTBD in 62% of the cases), while we did not observe such bias for the left and right MTBD with increasing off-axis distance (*SI Appendix*, Fig. S4 *H* and *I*).

However, we also found significant quantitative differences between the stepping of MTBDs and AAA rings, while the step-size distributions of both MTBDs were identical (Fig. 2*C*). For example, the AAA ring, on average, took slightly larger forward steps (22.2 nm) compared to the MTBD (18.8 nm for both MTBDs combined). Moreover, the AAA ring took fewer backward steps (14%) compared to the MTBD (21% and 19% for the blue- and red-labeled MTBD, respectively). In addition, focusing on steps along a single protofilament without any off-axis stepping component (Fig. 2 *D–F*), we detected steps with an ~8-nm periodicity for the MTBDs but not for all the steps of the AAA ring. The difference in step-size distributions of MTBD and AAA ring also held true when we imaged the three domains individually with higher temporal resolution (110-ms acquisition time instead of 330 ms) so that close to 100% of all steps were detected (*SI Appendix*, Fig. S3). Moreover, we also observed this difference in step-size distribution among AAA ring and MTBD for dyneins moving along axonemes (*SI Appendix*, Fig. S3). Thus, these results show that the two MTBDs exhibit identical movements, while the AAA ring and the MTBD do not, indicating more complicated movements rather than a simple rigid body translation of the entire motor domain.

Independent Stepping of the MTBD and the AAA Ring. Given the difference in on-axis step sizes and percentages of forward and backward steps of the AAA ring and MTBD, we next examined the timing of the steps of these domains (Fig. 3*A*). When the MTBD takes a short step (4 to 12 nm, centered around the dimension of a tubulin subunit [8 nm]), the AAA ring on the same motor domain displays an evident simultaneous step only ~60% of the time. Thus, not every step of an MTBD results in the relocation of the AAA ring on the same motor domain. However, when the MTBD stepped by distances of >20 nm (corresponding to distances of approximately three or more tubulin subunits), the probability of simultaneous stepping of the AAA ring increased to >90% (Fig. 3*B*). Collectively, these results might be explained by flexibility between these domains; when the MTBD takes a short step, the stalk can adjust its angle relative to the AAA ring,
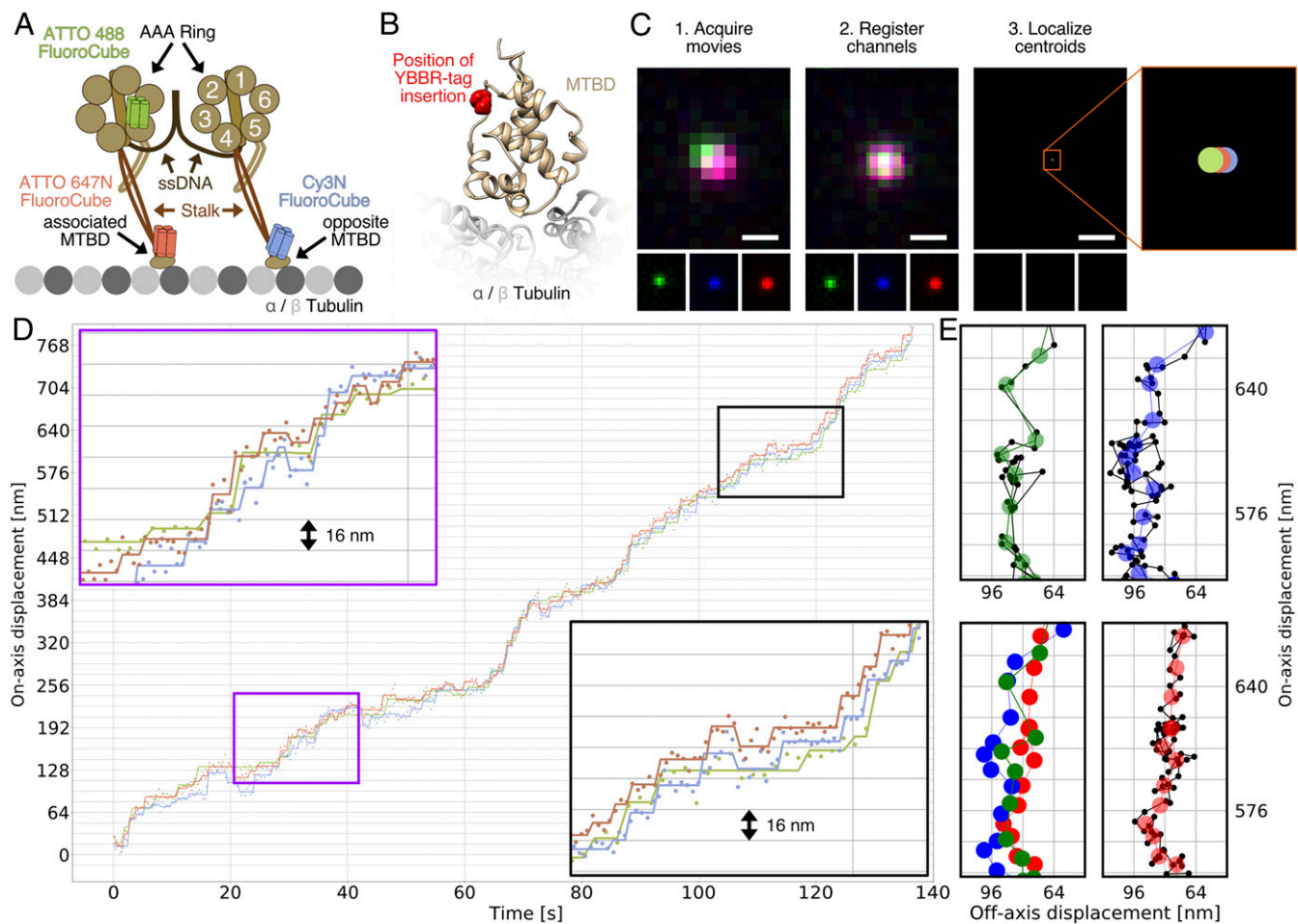
Fig. 1. Three-color stepping trace of dynein. (*A*) Schematic of design of three-color dynein. Each of the two motor domains of dynein is labeled individually and dimerized using reverse-complementary single-stranded DNA [black, attachment via SNAP-tag (39, 41)]. The MTBD of each motor domain and one of the two AAA rings are labeled with FluoroCubes (35). For one motor domain, the AAA ring is labeled with a six-dye ATTO 488 FluoroCube [green, attachment via HALO-tag (40)] and the MTBD (termed associated MTBD) is labeled with a six-dye ATTO 647N FluoroCube [red, attachment via YBBR-tag (41)]. For the other motor domain only the MTBD is labeled (termed opposite MTBD) with a six-dye Cy3N FluoroCube [blue, attachment via YBBR-tag (41)]. More details about construct design and labeling can be found in *Materials and Methods*. ssDNA, single-stranded DNA. (*B*) Structure of a yeast cytoplasmic dynein MTBD (gold) bound to tubulin (gray) [Protein Data Bank ID code 6KIQ (56)]. The exact position of the YBBR-tag insertion is shown as red spheres. (*C*) Workflow to collect three-color dynein stepping data. The top micrographs show a merge of all three colors while the bottom row shows each color separately. More details on data collection can be found in *Materials and Methods*. (Scale bars, 500 nm.) (*D*) Raw stepping data with position along the on-axis versus time of a three-color dynein heterodimer (colored dots) with detected steps (colored lines). (*Insets*) A magnified view of the area in the black and purple boxes. All other stepping traces were deposited on Zenodo at https://doi.org/10.5281/zenodo.4321962 (54). (*E*) Stepping trace in *xy* space for the magnified view in the black box of *D*. Raw data are shown as black dots together with the fitted position as circles in the respective color of each domain. The bottom left shows an overlay of the fitted stepping positions for all three domains.

resulting in little axial displacement of the AAA ring. However, longer MTBD steps can only be accommodated by a displacement of the AAA ring along the microtubule axis.
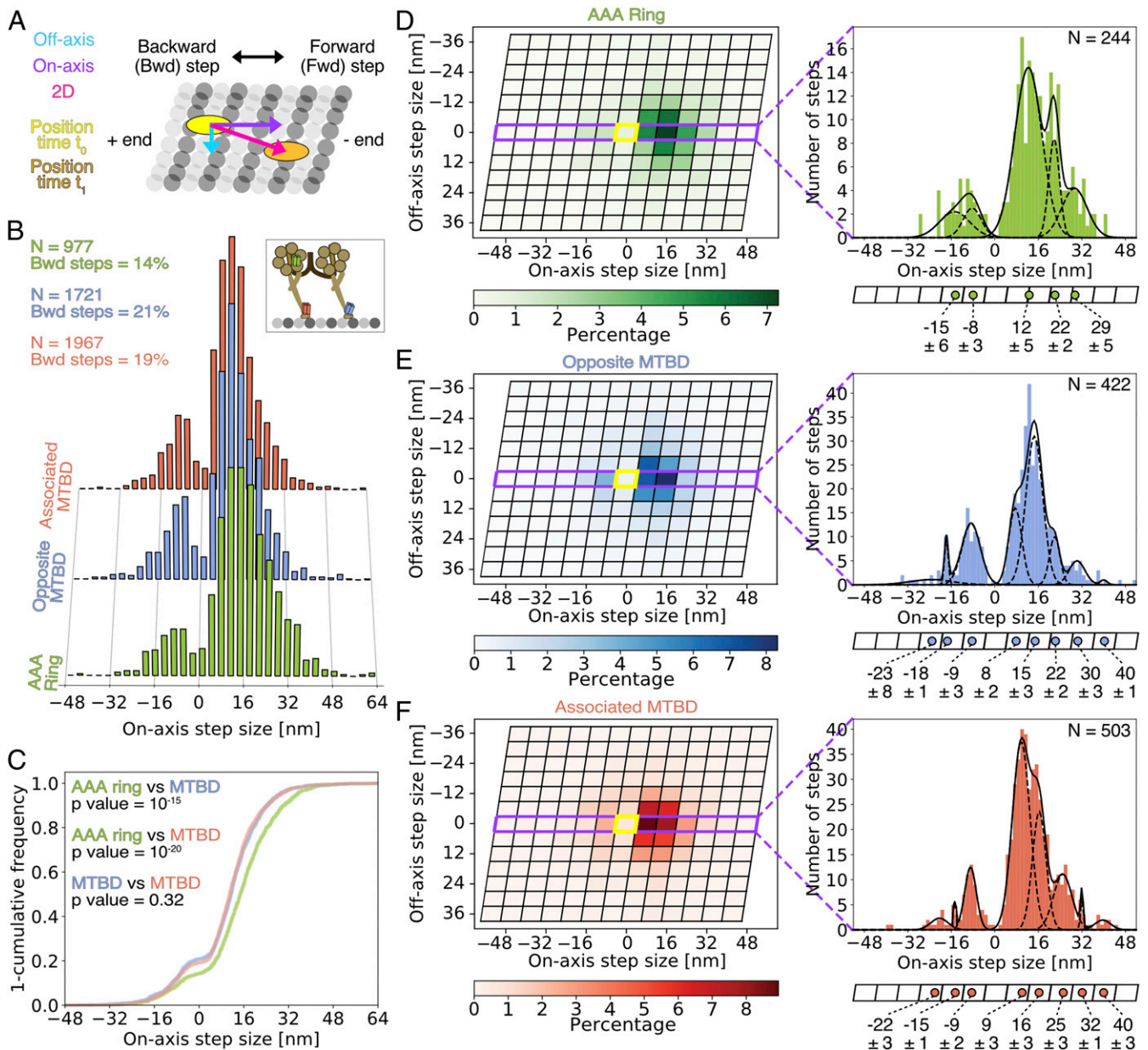
We also examined how often the MTBD on one motor domain steps at the same time as the AAA ring on the other motor domain and found, as expected, that a step of a MTBD of one motor domain does not necessarily result in the axial displacement of the AAA ring on the other motor domain (*SI Appendix,* Fig. S5 *A–C*).

Next, we focused our analysis on the direction and dimensions of the simultaneous steps of AAA ring and MTBD of the same motor domain (Fig. 3*B*). We found that the relative step sizes and directions were not always the same (Fig. 3 *C* and *D*). Although in most cases both domains stepped forward (Fig. 3 *C* and *D*, quadrant II), we observed cases in which the domains took steps in opposite directions; e.g., the MTBD takes a short backward step while the AAA ring moves slightly forward (Fig. 3 *C* and *D*,

quadrant IV), and vice versa (Fig. 3 *C* and *D*, quadrant I). The least likely event is for the MTBD to step forward and the AAA ring to move backward (Fig. 3 *C* and *D*, quadrant I). Overall, the correlation between on-axis steps of the AAA ring and the MTBD on the same motor domain indicates that the AAA ring takes, on average, larger forward steps and fewer backward steps than the MTBD (Fig. 3*C*) when both step simultaneously. In conclusion, AAA ring and MTBD do not necessarily advance along the track at the same time and over the same distance, further supporting the idea that they are not rigidly connected bodies.

Relative Positions of the AAA Ring and the MTBD. To investigate how the AAA ring and the MTBD move relative to each other, we examined the relative positions between green-labeled AAA ring and red-labeled MTBD of the same motor domain. On average, the MTBD was positioned in front of the AAA ring (closer to the microtubule minus end) (*SI Appendix,* Fig. S5 *D–L*). This finding

Niekamp et al.
Three-color single-molecule imaging reveals conformational dynamics of dynein undergoing motility

PNAS | 3 of 11
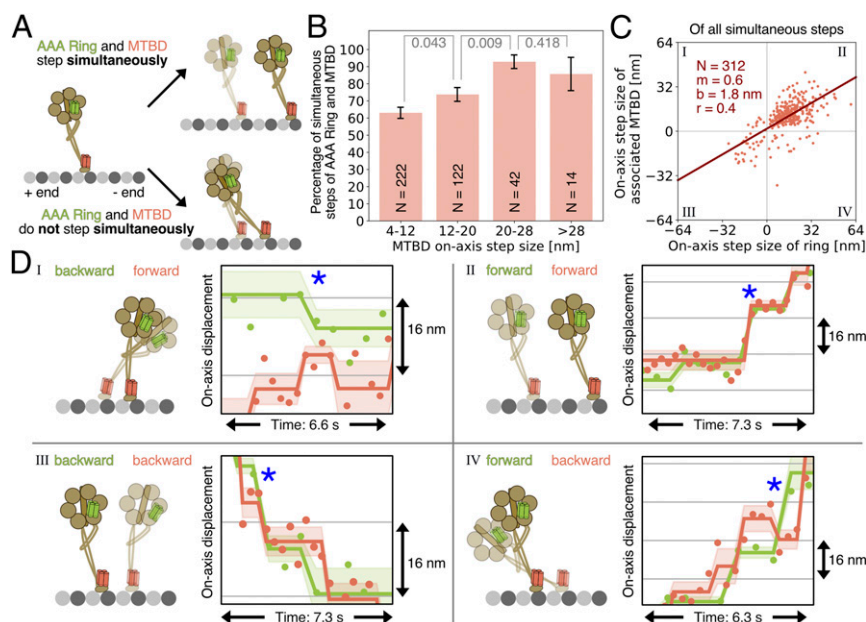https://doi.org/10.1073/pnas.2101391118

Fig. 2. Two-dimensional analysis of AAA ring and MTBD stepping. (*A*) Microtubule lattice (gray circles) with plus and minus ends and the definition of forward and backward as well as two-dimensional, on- and off-axis steps. (*B*) Histogram of on-axis step sizes of dynein's AAA ring (green), the MTBD (blue) on the opposite motor domain, and the MTBD (red) of the same motor domain (associated MTBD). Additional fitting parameters are shown in *SI Appendix*, Table S1. (*C*) Cumulative frequency plot for on-axis step sizes of dynein's AAA ring (green), the opposite MTBD (blue), and the associated MTBD (red). *P* values are a relative comparison among all three distributions and were calculated using Kolmogorov–Smirnov statistics. (*D–F*) (*Left*) Two-dimensional stepping distributions in *xy* space of (*D*) dynein's AAA ring (green), (*E*) the opposite MTBD (blue), and (*F*) the associated MTBD (red) mapped on a microtubule lattice. (*Right*) On-axis step-size distributions focusing on a single protofilament (purple box; no off-axis step). Gaussian fits to step-size histograms reveal multiple major peaks. Peak positions are displayed below the corresponding histogram. The microtubule lattice is based on a flattened 13-protofilament microtubule. A flattened microtubule representation was used since our data only report steps in the *xy* (horizontal) plane but not in the *z* (vertical) direction. Here, each parallelogram represents a tubulin dimer consisting of one copy of α- and β-tubulin. The yellow parallelogram represents the tubulin dimer at which the domain was located prior to the step.

is consistent with static electron microscopy data of dynein bound to microtubules (2, 34). However, there was no preferential position of the two MTBDs or between the MTBD and AAA ring along the off-axis of the microtubule (*SI Appendix*, Fig. S5 *D–L*).

Next, we calculated the angle between the stalk and microtubule based on the relative positions of the AAA ring and MTBD. To calculate the stalk-microtubule angle ω, we used the on-axis distance between the AAA ring and MTBD of the same motor domain and assumed a fixed length of the dynein stalk (Fig. 4*A*).

We found a wide distribution of angles averaging at 80.5° (Fig. 4*B*), further supporting the idea of a high flexibility within the dynein motor domain.

Next, we asked whether the stalk-microtubule angle ω is different for the leading and trailing motor domains (Fig. 4*C*). Comparing the average angle for both cases, we found that the angle ω for the leading motor domain (red MTBD leading; 71.8°) was significantly smaller than for the trailing motor domain (red MTBD trailing; 90.0°) (Fig. 4*D*). We also calculated the stalk-microtubule angle ω

Niekamp et al.
Three-color single-molecule imaging reveals conformational dynamics of dynein
undergoing motility

Fig. 3. Independent stepping of AAA ring and MTBD on the same motor domain. (*A*) The AAA ring and MTBD on the same motor domain can either step simultaneously (*Top*: both domains move along the on-axis) or not step simultaneously (*Bottom*: only MTBD moves while the AAA ring remains at the same on-axis position). (*B*) Histogram showing how often the AAA ring steps at the same time as the associated MTBD (red) as a function of the MTBD on-axis step size. N refers to the total number of steps for each condition. The error bars show the bootstrapped SEM. The *P* values (gray) were calculated with a two-tailed *z* test. (*C*) Correlation of on-axis step sizes of the AAA ring and the associated MTBD (red) when they step at the same time. Each dot represents a single step. Red line shows linear fit. N is the sample size. m is the slope. b is the y-intercept. r is the Pearson correlation coefficient. (*D*) Example on-axis traces for each of the four quadrants (I, II, III, and IV) defined in *C*, accompanied by a diagrammatic representation where the initial position is shown with decreased opacity. The blue asterisks indicate the time at which the AAA ring and MTBD moved simultaneously. All traces are raw stepping data with position along the on-axis versus time of a three-color dynein heterodimer (colored dots) with detected steps (colored lines). The opaque lines show the SD along the on-axis for each step. Note that the blue channel was removed for clarity.

as a function of inter-MTBD on-axis distance and found that the angle of the trailing motor domain increases with increasing separation of the two MTBDs, while the angle of the leading motor domain decreases (Fig. 4 *E* and *F*). Taken together, these data reveal flexibility between the AAA ring and MTBD on the same motor domain and that the leading motor domain typically adopts a more acute stalk-microtubule angle compared with the trailing motor domain.

Dynein Adopts a Large Variety of Conformations. Three-color imaging enabled us to determine the relative positions of the AAA ring and the two MTBDs along the on-axis of the microtubule. Permuting through all possible orders of three colors leads to a total of six different domain orderings, each of which can be associated with four potential conformational states of dynein (Fig. 5*A* and *SI Appendix*, Fig. S6 *A* and *B*). To determine the relative frequency of domain orders, we quantified how often each of the six domain orders occurs during all stepping traces. We found that dynein can adopt all six domain orders to a varying degree (Fig. 5*B*). The two most common domain orders were the ones in which both MTBDs are leading the green-labeled AAA ring (51% combined), followed by the two domain orders in which the AAA ring is positioned between both MTBDs (32% combined), and followed by the two domain orders in which the AAA ring is leading (17% combined). Interestingly, based on previous studies (1) we would not have predicted the two domain orders in which the green-labeled AAA ring is leading. Together, the observation of a large variety of domain orders suggests that dynein can adopt a large variety of conformational states during motility (*SI Appendix*, Fig. S6 *A* and *B*).

We next asked how frequently dynein transitions to a new domain order after a step occurred. If conformational states were random, we would have expected that 1/6 (~17%) will remain in the initial domain order after one step and only 1/36 (< 3%) will still have the same domain order after the first and second step. However, we found that dynein tends to remain in its same domain order after a step (Fig. 5*C* and *SI Appendix*, Fig. S5*J*), although some states are more persistent than others. For example, the two domain orders in which the green-labeled AAA ring is leading are the least stable and more likely to transition to other domain orders in which the MTBDs are leading. This observation of a persistence of domain orders agrees with previous observations in which the AAA rings of dynein were reported to infrequently pass each other (29). We also measured how often a step of any of the labeled domains was followed by a step of the same or another domain. The most common outcome was that one MTBD moves after the other (*SI Appendix*, Fig. S5*K*), which is again consistent with the observation that the two dynein AAA rings tend to step in an alternating fashion (29, 30). In summary, dynein's AAA ring and the two MTBDs often move in an alternating fashion and are less likely to pass each other, resulting in a persistence of a given domain order over multiple steps.

Simulation of Dynein Motility. The observation of six three-color domain orders shows that dynein can adopt a large variety of conformations when moving along microtubules. However, we lack information on the location of the second AAA ring. Thus, we turned to Monte Carlo simulations to obtain more insights into dynein conformations during motility and to uncover the minimum characteristics required to describe dynein movement. Using our experimental data as input, we simulated the stepping of both AAA rings and both MTBDs along microtubules (Fig. 6*A* and Movie S3) by assigning probabilities to step sizes, stepping directions, and likelihoods of what kind of step will follow another, as described in *Materials and Methods*. We also applied a few rules that are based on our data of the three-color dynein
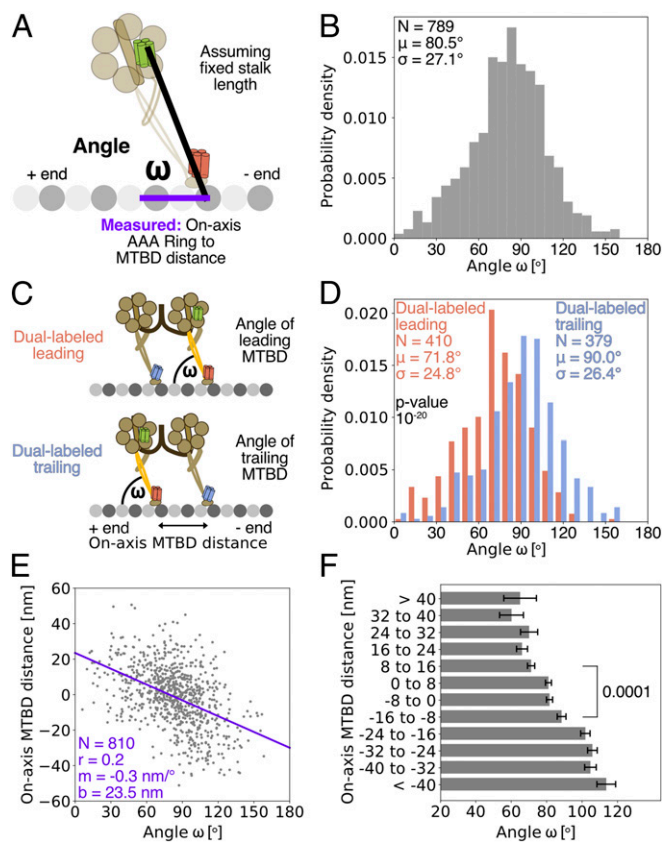
Fig. 4. Relative movement of AAA ring and MTBD on the same motor domain. (A) Schematic showing the definition of the angle ω between stalk and microtubule on-axis. Note that the angle is only calculated for the motor domain for which the AAA ring (green) and the MTBD (red) are both labeled. To calculate the angle ω we used the measured on-axis distance between the AAA ring and MTBD (purple line) and the fixed known distance from the MTBD to the center of the AAA ring (black line). (B) Histogram of stalk-microtubule angles ω. (C) Schematic showing definition of leading and trailing MTBD. (*Top*) Angle measurement for the dual-labeled motor domain leading (red MTBD leading). (*Bottom*) Angle measurement for the dual-labeled motor domain trailing (blue MTBD leading). (D) Histogram of stalk-microtubule angles ω if either the dual-labeled motor domain is leading (red) or trailing (blue). The P value was calculated with a two-tailed t test. (E) Correlation between stalk-microtubule angles ω and inter-MTBD on-axis distances at the single-molecule level (gray dots). Here, a positive value refers to a state in which the dual-labeled motor domain is leading, and a negative value refers to a state in which the dual-labeled motor domain is trailing. Purple line shows linear regression. N is the sample size. m is the slope. b is the y-intercept. r is the Pearson correlation coefficient. (F) Same data as in E but binned into 8-nm bins (size of one tubulin dimer). Error bar shows SEM. The P value was calculated with a two-tailed t test. In B and D sample size (N), average distance (μ), and its SD (σ) are given.

(Movies S4–S9). Specifically, 1) an on-axis distance-dependent bias to take more forward than backward steps (Fig. 2), 2) a distance-dependent bias to close the gap between the motor domains along the on- and off-axis when taking a step (*SI Appendix*, Fig. S4), 3) a higher probability for the trailing domain instead of the leading domain to take the next step (*SI Appendix*, Fig. S4), 4) a bias toward alternating stepping behavior (*SI Appendix*, Fig. S4), and 5) the relative movement between AAA ring and MTBD (changes in angle ω) (Fig. 4). However, we did not enforce specific distances between the two motor domains by setting cutoffs for on- and off-axis distance; in other words, the motor domains were not constrained by a connecting tether and stepped independently (Fig. 6A) according to the rules set above.

When we applied all these rules during the simulation, we could reproduce the experimental data for dynein stepping very well; the step-size distributions of AAA rings of the simulation were almost identical to those observed in experimental data (Fig. 2 and *SI Appendix*, Fig. S7). Interestingly, certain parameters that were not provided in the model agreed well with previous experimental observations. For instance, we did not provide input regarding the spacing of the AAA rings, except for the experimentally determined step-size distributions of the associated MTBDs and the relative movement (changes in angle ω) between the AAA ring and MTBD (Fig. 6A). Nevertheless, our simulation yielded inter-AAA ring distances (Fig. 6B) that were very similar to those observed in early reported stepping experiments in which both AAA rings were labeled (29, 30). In addition, we also found good agreement for the probability of passing and not passing steps for the AAA rings when we compared it to prior experimental data (29) without directly encoding this motion in the simulation (Fig. 6B).

However, if we ignored any of the above-listed rules during a Monte Carlo simulation the simulated dynein motility did not match current or previous experimental observations (*SI Appendix*, Fig. S8). For instance, if we did not apply the tendency for the motor domains to step closer toward each other along the off-axis (Fig. 6C and *SI Appendix*, Fig. S8B), but rather allowed the motor domains to move in either direction along the off-axis, the motor domains drifted apart >100 nm in some simulations. Moreover, if we fixed the angle ω between the AAA ring and MTBD the simulation produced a larger inter-AAA ring distance (~27 nm) than experimentally measured (~18 nm) (29) (Fig. 6C, *SI Appendix*, Fig. S6 D–L, and Movies S3, S9, and S10). Thus, encoding the experimentally derived set of rules and transition probabilities listed above is sufficient and necessary to recapitulate directed dynein motility using Monte Carlo simulations.

Since our three-color experimental data only captured the positions of one AAA ring and two MTBDs, the information regarding the location of the second AAA ring is missing. However, since our Monte Carlo simulation reproduced our and experimental data of others very well, we used this simulation to predict the positions of both AAA rings and MTBDs during motility. As a general validation of this approach, we compared the frequency of the experimental three-color domain orders (Fig. 5) to the frequency of three-color domain orders from the Monte Carlo simulations and found good agreement (*SI Appendix*, Fig. S6C). Considering the four moving parts (two AAA rings and two MTBDs in the homodimer), dynein can adopt 12 potential conformations (*SI Appendix*, Fig. S6 A and B). Of these 12 possible conformations, our simulation predicts that the first three conformations make up ~55% of the total, while the six least common conformations comprised <20% (Fig. 7 and *SI Appendix*, Fig. S6B). Overall, conformations in which the stalks did not cross were more common (~76%) than conformations in which the stalks cross one another (~24%). Interestingly, the eight conformations in which at least one motor domain has a stalk-microtubule angle of >90° were not predicted by previous models of dynein motility (1) but make up ~65% of all dynein conformations based on our simulation.

We next investigated how experimental errors, such as localization errors, rotational degrees of freedom of the FluoroCube, and missed steps due to temporal resolution constraints, might alter the conclusions of our Monte Carlo simulation. Using an average SD for the step detection of ~3.5 nm and a registration error of ~1 nm, we ran Monte Carlo simulations with an SD of 5 nm for the precision of each step. Using this approach, we tested whether other models with fewer or other dynein conformational states could explain the experimental data. Overall, we found that as few as four conformational states, together with experimental errors, could also explain the experimental data (*SI Appendix*, Fig. S9 and *Supplementary Note 1*). However, without the inter-MTBD distance dependent stalk-microtubule angle changes observed in this study (Fig. 4) we could not recapitulate
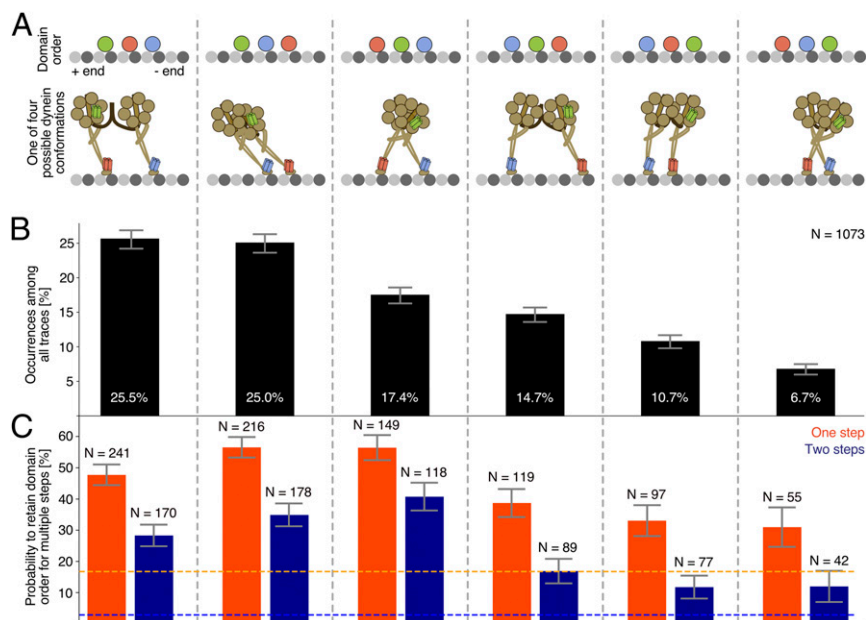
Fig. 5. Frequency of domain orders of AAA ring and both MTBDs. (*A*) Schematic of all six possible domain orders along the microtubule on-axis. (*Top*) Small, gray circles show tubulin while the larger green, blue, and red circles represent the AAA ring, the opposite MTBD, and the associated MTBD, respectively. For instance, to be classified as the very left domain order, the opposite MTBD (blue) must be closest to the microtubule minus end, followed by the associated MTBD (red) and followed by the AAA ring (green). Note that the absolute distance between domains is irrelevant. (*Bottom*) One of the four possible dynein conformations based on the three-color domain orders. Other possible conformations are shown in *SI Appendix*, Fig. S6. (*B*) Histogram of occurrence of each of the six possible domain orders with sample size N. The error bars show the bootstrapped SEM. (*C*) Probability to retain domain order after one (orange) or two (blue) steps. Here, a step refers to the movement of at least one of the three domains. The orange and blue dotted lines indicate the probability to retain the domain order after one (orange) or two (blue) steps if transitions were random. The sample size N refers to the total number of all domain order transitions that occurred after the motor took a step out of its current domain order. The error bars show the bootstrapped SEM. A more detailed analysis of transitions between domain orders is given in *SI Appendix*, Fig. S5.

the experimental data (*SI Appendix*, Fig. S9 *D* and *E*). Taken together, our experimental data in combination with the Monte Carlo simulation provides a model of the distribution of dynein conformations during motility.
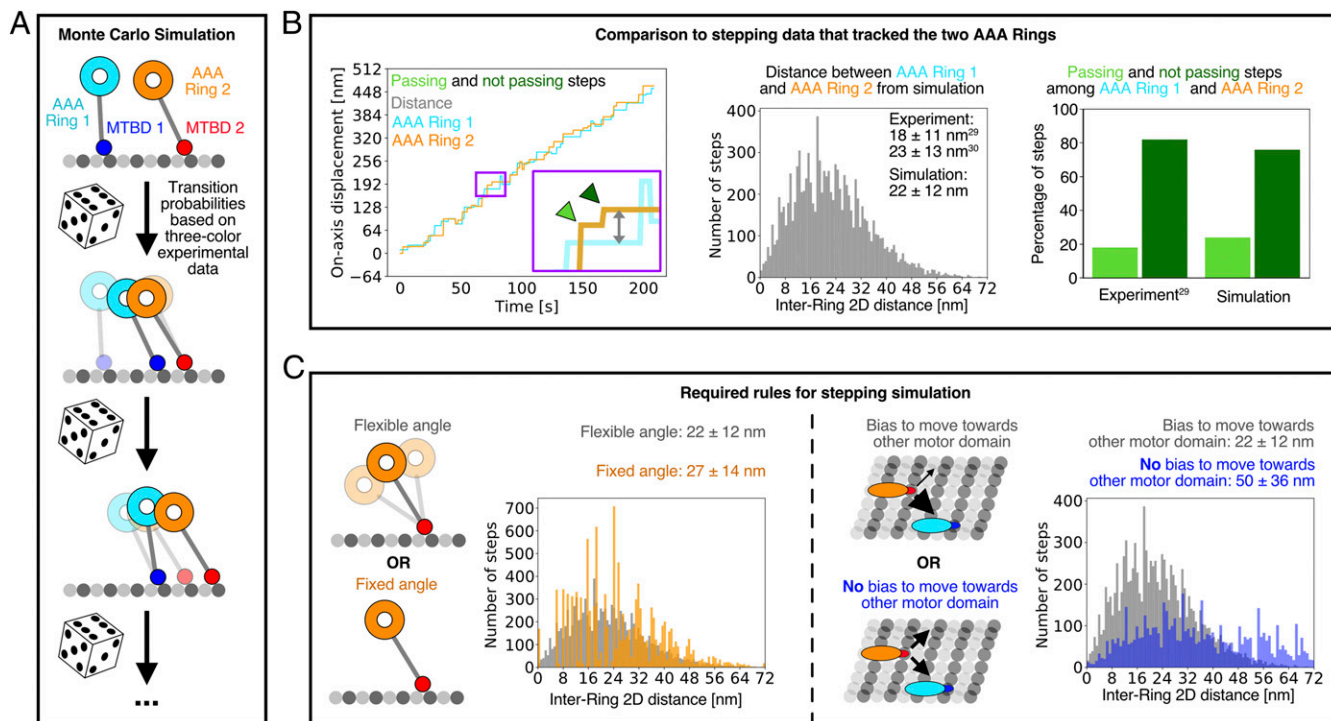
Discussion

Previous dynein stepping experiments have measured the positions of the AAA rings (29, 30). Here, we have been able to track the movements of both MTBDs, in combination with one AAA ring. Several technical challenges had to be overcome to make this measurement. First, the small 14-kDa MTBD (22) had to be labeled without perturbing motor function. For this, the common HALO-tag (40) and SNAP-tag (39) are nonideal, since they are twice as large as the MTBD. However, we found that a 14-amino-acid-long YBBR-tag (41) could be inserted into loop 5 of the MTBD and then labeled with a DNA FluoroCube (35) without perturbing wild-type function. Second, tracking three colors for a prolonged time is not easily achievable with conventional dyes due to photobleaching, as even the photobleaching of one dye terminates the measurement. However, using DNA FluoroCubes, which are up to 50-fold more photostable than conventional organic dyes, enabled long-term tracking of many steps. Third, the distances between three colors had to be measured with nanometer accuracy. For this, we extended our previously published two-color data collection and imaging analysis pipeline (36) to three colors. All three technical advances described above were essential to accurately measure the positions of three domains of dynein as the motor undergoes hundreds of steps along a microtubule. These measurements provided insights into the stepping behavior and conformational states of dynein, as discussed below.

Flexibility within the Motor Domain Allows Dynein to Adopt Many Conformational States. Our experimental data of the three-color-labeled dynein, combined with Monte Carlo simulations, show that dynein

can adopt a large variety of conformations, many of which were not considered in prior stepping models of dynein (1, 29, 30). These conformational states presented in Fig. 7 are most likely enabled by angular changes to the stalk that spans between the AAA ring and the MTBD. A wide range of stalk angles have been previously measured by electron microscopy (2, 34) and polarization microscopy (33). The polarization microscopy study also observed hinging of the stalk, which allows the AAA ring to rotate while dynein is moving along microtubules (33). This observation is in good agreement with our observations of flexible movement between AAA ring and MTBD. However, the average angles between stalk and microtubule determined by cryo-electron microscopy by Imai et al. (34) and Can et al. (2) were ~42° and ~55°, respectively, and are smaller than what we measured for the leading (72°) and trailing (90°) motor domain. One explanation for this difference might be that our C-terminal fluorescent label on the AAA ring is not in the center but rather on the side of the AAA ring, which is closer toward the minus end and thus could bias the angle toward larger values. Using structural information, we estimated an offset of ~3 nm from the center of the AAA ring to the position of the HALO-tag (C terminus of dynein) along the on-axis and applied this correction to our data analysis pipeline. Taking this correction into account, we measured a stalk-microtubule angle of 67.1° for the leading motor domain and 83.3° for the trailing motor domain. Interestingly we estimated a stalk-microtubule angle of ~65° in a recent cryo-electron tomography structure of dynein (42), which is in good agreement with our offset corrected angle values. While this potential offset changes the values of the angles, it does not change the general conclusion of a considerable relative movement between AAA ring and MTBD.

In addition to measuring an average angle, we could obtain information on how the stalk angle is dependent upon the separation of the two MTBDs and other parameters that change as dynein steps (Fig. 4 and *SI Appendix*, Figs. S4, S5, and S10). For

Niekamp et al.
Three-color single-molecule imaging reveals conformational dynamics of dynein undergoing motility

PNAS | 7 of 11
https://doi.org/10.1073/pnas.2101391118

Fig. 6. Monte Carlo simulation of dynein motility. (*A*) Using the three-color experimental data as input the positions of both MTBDs and both AAA rings can be simulated using Monte Carlo simulation. (*B*) Comparison of Monte Carlo–simulated dynein motility to previously published experimental data for which both AAA rings were tracked (29, 30). (*Left*) Example stepping traces from Monte Carlo simulation of both AAA rings. (*Middle*) Histogram of two-dimensional (2D) distance between both AAA rings compared to previously measured interring 2D distance (29, 30). (*Right*) Passing and not passing steps among the two AAA rings based on simulations compared to previously measured data (29). (*C*) By running Monte Carlo simulations, the importance of different rules on dynein motility can be evaluated. Here, the influence of two rules on the 2D distance between both AAA rings was tested. The influence of a relative movement among AAA ring and MTBD. Simulations with either a variable stalk-microtubule angle (*Left*, gray) or with a fixed stalk-microtubule angle (*Left*, orange) were run. The influence of a distance-dependent bias to close the gap between the motor domains along the off-axis. Simulations with either a bias to step toward each other (*Right*, gray) or without a bias to step toward each other (*Right*, blue) were run. Note that the distance distribution for the flexible angle is from the same data as in *B*. The influence of other rules on dynein motility are shown in *SI Appendix*, Fig. S8. (*B* and *C*) One hundred simulations for each condition with more than 10,000 steps were performed. More details on the Monte Carlo simulation can be found in *Materials and Methods* and *SI Appendix*, Figs. S7 and S8 and Movies S3–S10.

instance, when the MTBDs are relatively close to each other (8 nm apart, the spacing between tubulin dimers), we found that the stalk-microtubule angles of both motor domains were relatively similar (Fig. 4 *E* and *F*). However, when the MTBDs are further apart (>16 nm, two or more tubulin dimers), the motor domains tilt toward each other, resulting in a split-like conformation

in which the AAA rings are closer together than the MTBDs (see Fig. 7, topmost left and topmost right states). The tilting of the two motor domains has also been observed in another study that measured the rotation of the AAA ring and found larger rotations with larger steps of the motor domain (33). Since we were able to track individual dyneins during many steps, we could also observe that the
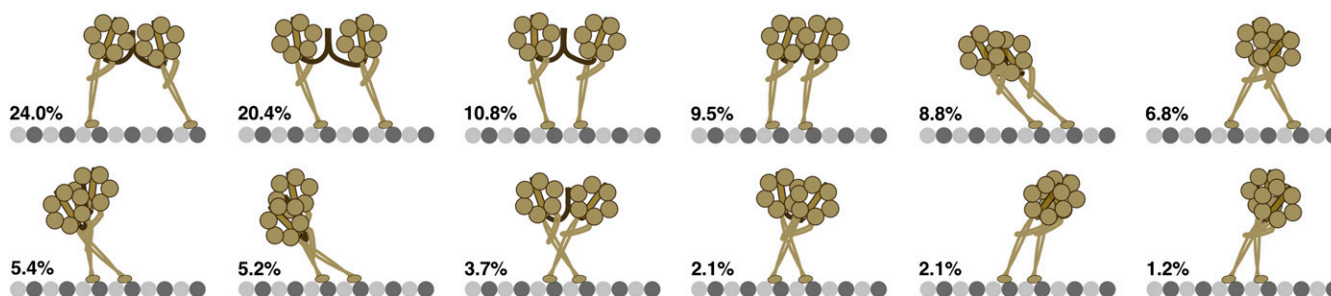
Fig. 7. Model of dynein conformations. Monte Carlo simulation of dynein motility was used to determine the frequency of all 12 possible dynein conformational states (positions of AAA rings and MTBDs relative to the microtubule on-axis). Here, the occurrence of all 12 states is ordered from most common to least common (from top left to bottom right). Note that the absolute distance between the four domains (both AAA rings and both MTBDs) is irrelevant and that only the relative proximity of all four domains to the microtubule minus end determines the classification into conformational states. Moreover, we only show conformations for changes along the on-axis and are ignoring differences along the off-axis. We note that when we added experimental noise we found that as little as four conformational states are sufficient to explain the experimentally observed states. A more detailed analysis of the influence of experimental errors on the distribution of conformational states of dynein is shown in *SI Appendix*, Fig. S6 and S9 and discussed in more detail in *Discussion* as well as in *SI Appendix, Supplementary Note 1*.

stalk-microtubule angle changes as dynein moves along its track (see model for dynein stepping in *SI Appendix*, Fig. S10). For example, when the trailing motor domain passed the leading motor domain it often changed its angle from a steep to a shallower angle (pivot-like motion) (Fig. 3 *C* and *D*). In summary, while other studies looked at distributions of static dynein and also observed flexibility within dynein motor domain, this study observed the flexibility of actively moving dynein, giving insights into motility.

By tracking one AAA ring and two MTBDs we could derive more information on dynein conformational states during motility than could be inferred in prior studies that measured the AAA rings (29, 30, 32). By combining our experimental data with Monte Carlo simulations we estimated the frequencies of 12 possible conformational relationships of the two AAA rings and the two MTBDs. Overall, these data suggest that states in which the MTBDs are further apart than the AAA rings are more common than vice versa. In addition, we find that for the leading motor domain the MTBD is typically leading the AAA ring, while the trailing motor domain has an almost equal distribution of either AAA ring leading or MTBD leading. Moreover, our data show that the stalks of the dynein homodimer are rarely crossed; in other words, if the MTBD of motor domain 1 is leading the MTBD of motor domain 2, then it is very likely that the AAA ring of motor domain 1 is also leading the AAA ring of motor domain 2. Interestingly, we found that dynein only changes its conformational state after a step occurred in ~50% of all cases (Fig. 4) and that if dynein transitions between two states it most likely switches between the two most common conformational states by a pivot-like transition (AAA ring and MTBD switch the lead) within the motor domain (Figs. 5 and 7, two upper left states). We could also demonstrate through simulation that the ability to adopt these conformational states requires a flexibility for the angle between the stalk and microtubule; if we fixed the angle between stalk and microtubule, as indicated in some dynein stepping models (1), dynein can only adopt 2 of the 12 possible conformations (*SI Appendix*, Fig. S6 and Movies S3, S9, and S10). While the flexible movement among AAA ring and MTBD is essential to explain the experimental data, even if one considers limitations in spatio-temporal resolution (Fig. 7 and *SI Appendix*, Fig. S9), it is possible that some of the less-frequent conformational states predicted based on our experimental data can be explained by experimental noise. Our present work suggests that a minimum of at least four conformational states of dynein are needed to explain the experimental data (*SI Appendix*, Fig. S9 and *Supplementary Note 1*). However, since we used the upper bound for the experimental noise when we determined the minimum number of conformational states, it is likely that we would find a larger number of minimal conformational states if we used a lower estimate for the experimental error (e.g., an SD of 3 nm instead of 5 nm). Thus, dynein likely adopts between 4 and 12 conformational states. An exact confirmation of those states would require future studies with even higher spatial resolution and four-color labeling so that both AAA rings and both MTBDs can be tracked simultaneously. Nevertheless, the general conclusions of the dynein conformational states discussed above, such that the MTBDs are further apart than the AAA rings, remain unaffected. Overall, our combination of three-color imaging and Monte Carlo simulation of dynein motility provides insights into the frequency as well as transitions between dynein conformational states and shows that a high degree of flexibility within the dynein motor domain is essential to achieve these conformations.

The AAA Ring Follows Exploratory Stepping of the MTBD. The stepping of the MTBD is initiated by ATP binding and a rotation of the AAA ring caused by the bending of the linker, dynein's mechanical element (1, 23, 25–27). The MTBD then is believed to execute a Brownian search followed by a rebinding to a new tubulin subunit. By tracking the MTBD and AAA ring simultaneously, we found

that this search can have many different outcomes for the transition of the entire motor domain. In some cases, the MTBD can move (forward or backward) without a translation of the AAA ring, and even if both domains step simultaneously they can take differently sized steps (Figs. 2 and 3).

These results are most consistent with flexibility within the dynein motor domain as opposed to rigid body movements of the motor domains. For example, relative movement between AAA ring and MTBD would allow the MTBD to take a short step, either backward or forward, while the AAA ring rotates and does not translate significantly along the long-axis direction (Fig. 3*A*). However, if the MTBD takes a larger step after a Brownian search, the AAA ring on the same motor domain will be forced to follow, because the step cannot be accommodated solely by an angular change between the AAA ring and MTBD. However, since our acquisition approach likely failed to detect some of the AAA ring steps (*SI Appendix, Supplementary Note 1*), it is possible that the percentage of independent MTBD steps without AAA ring translocations is lower than we report in this study (Fig. 3*B*). This might also explain why we measured similar behavior for simultaneous steps of the AAA ring and the associated as well as opposite MTBD (Fig. 3*B* and *SI Appendix*, Fig. S5*B*). Nevertheless, we have shown that the relative movement between AAA ring and MTBD is an essential component of dynein motility (Fig. 6 and *SI Appendix*, Figs. S6 and S9 and *Supplementary Note 1*). This relative movement might also explain why we could not detect steps with 8-nm periodicity for the AAA ring while we detected steps following the 8-nm periodicity of tubulin for the MTBDs (Fig. 2). Thus, our data suggest that the AAA ring is essential to initiate and power the step, while the Brownian search of the MTBD and the flexibility of the stalk determines the step and which parts of the motor domain translocate (only MTBD or MTBD and AAA ring). In future studies it will be interesting to see how the relative movement of the AAA ring and MTBD correlates with models of the mechano-chemical cycle of dynein (43). One possibility is that ATP binding (linker bending) and phosphate release (linker straightening) drive the tilting of the AAA ring relative to the MTBD.

The sometimes differently sized steps of the AAA ring and the MTBD and the large variety of conformational states are strikingly different from other motor proteins such as kinesins, where the motor domain takes regular, 16-nm, and almost exclusively forward steps (28, 44). Dynein's inherent flexibility and ability to step in so many different ways might explain why a single dynein is more efficient than a single kinesin in circumventing obstacles such as microtubule-associated proteins (45, 46).

Dynamic, Multicolor Imaging Is Suitable for Studying Large Molecular Machines. Distance measurement between protein domains has been extensively investigated using Foerster resonance energy transfer (FRET) (47). However, FRET is typically limited to short distances of 2 to 8 nm. In contrast, the multicolor measurements described here are not limited to any distance and thus can be applied to macromolecular complexes of any size to obtain direct distance relationships. Together with DNA FluoroCubes (35), which provide a mechanism for following dynamics over long periods of time, the approach described in this work can be useful to investigate conformational changes of other multidomain proteins or macromolecular complexes. For instance, the multicolor approach could be applied to study conformational changes of chaperones during the refolding of client substrates. We also envision that our approach could be applied to molecular machines that operate on tracks other than microtubules such as DNA. For example, the high-resolution multicolor approach could be used to investigate how chromatin remodelers interact with nucleosomes along DNA. Finally, we anticipate that the framework provided in this work can be extended to four colors, which will further expand the reference points for investigating intra- and interprotein dynamics.

Niekamp et al.
Three-color single-molecule imaging reveals conformational dynamics of dynein undergoing motility

PNAS | 9 of 11
https://doi.org/10.1073/pnas.2101391118

Materials and Methods

Flow-Cell Preparation. Flow-cells were assembled as described in (36). Briefly, we cut custom three-cell flow chambers out of double-sided adhesive sheets (Soles2dance 9474-08x12, 9474LE 300LSE; 3M) using a laser cutter. We then used these three-cell flow chambers together with glass slides (12-550-123; Thermo Fisher Scientific) and 170-μm-thick coverslips (474030-9000-000; Zeiss) to assemble the flow cells. Prior to assembly, coverslips were cleaned in a 5% vol/vol solution of Hellmanex III (Z805939-1EA; Sigma) at 50 °C overnight and washed extensively with Milli-Q water afterward.

Assembly of DNA FluoroCubes for Dynein Labeling. FluoroCubes were assembled as described in ref. 35 and *SI Appendix, Supplementary Information Methods*.

Dynein Expression, Purification, and Labeling. We used recombinant *Saccharomyces cerevisiae* cytoplasmic dynein (Dyn1) truncated at the N terminus (amino acids 1219 to 4093) as a monomeric version expressed in a yeast strain with the following genotype: MATa his3-11,5 ura3-1 leu2-3,112 ade2-1 trp-1 PEP4::HIS5 pGAL-ZZ-TEV-SNAPf-3XHA-D6-DYN1(MTBDL5:YbbR)-gsDHA for all our stepping experiments (VY1067). This construct has a N-terminal SNAP-tag (39, 41), a C-terminal Halo-tag (40), and a YBBR-tag (41) inserted into loop 5 of the MTBD flanked by three glycines on either side (inserted as GGG-TVLDSLEFIASKLA-GGG between T3173 and L3174). In addition, we used the VY208 (MATa his3-11,5 ura3-1 leu2-3,112 ade2-1 trp-1 PEP4::HIS5 pGAL-ZZ-TEV-sfGFP-3XHA-D6-DYN1-gsDHA) construct as a wild-type control for our velocity and processivity analysis. Expression of dynein, either VY208 or VY1067, and yeast lysis were executed as previously described (15, 36). The purification and labeling of dynein are described in detail in *SI Appendix, Supplementary Information Methods*.

Microtubule Preparation. The tubulin used in this work was purified and polymerized as described in ref. 48. Briefly, we used unlabeled tubulin and biotinylated tubulin that were mixed at an approximate ratio of 20:1 in BRB80 (80 mM Pipes [pH 6.8], 1 mM EGTA, and 1 mM MgCl$_2$). To start the polymerization reaction guanosine 5′-triphosphate was added to 1 mM and the solution was incubated for 15 min in a 37 °C water bath. Then, 20 μM of Taxol (T1912; Sigma) was added and the mixture was incubated for another 2 h at 37 °C. At the start of each experiment, microtubules were spun over a 25% sucrose cushion in BRB80 at ~160,000 × *g* for 10 min to remove unpolymerized tubulin and small filaments.

Preparation of Flow Cells with Dynein. The flow chambers for the single-molecule assay were prepared as previously described (49). To conduct all experiments described in this study, we prepared four slightly different types of environments: 1) For the majority of experiments we used biotinylated microtubules as tracks and a low ATP concentration (3 μM), 2) for one experiment we used axonemes as tracks and a low ATP concentration (3 μM) (*SI Appendix, Fig. S3*), 3) for another experiment we used biotinylated microtubules as tracks and added 1 mM ADP to allow dynein to bind tightly to microtubules (*SI Appendix, Fig. S2*), and 4) for one experiment we used biotinylated microtubules as tracks and a high ATP concentration (1 mM) (*SI Appendix, Fig. S2*). The preparation of flow cells with dynein was modified from refs. 35 and 36 and is described in detail in *SI Appendix, Supplementary Information Methods*.

Fluorescent Beads for Image Registration. To register the three channels, we used TetraSpeck beads (T7279; Thermo Fisher Scientific) based on a previously described protocol for two-color image registration (36). To this end, we prepared one of the three flow chambers of our flow cells with dynein (or with the DNA-origami nanoruler; *SI Appendix, Fig. S1*) and another flow chamber on the same flow cell with TetraSpeck. The beads were immobilized by adding 10 μL of 1 mg/mL Poly-D-lysine (P6407; Sigma) in Milli-Q water to the flow cell, followed by a 3-min incubation and a wash with 20 μL of BRB80 (80 mM Pipes [pH 6.8], 1 mM EGTA, and 1 mM MgCl$_2$). Afterward, we added 10 μL of 1:300 diluted TetraSpeck beads in BRB80 and incubated for 5 min. Finally, the flow cell was washed with 40 μL of BRB80.

DNA-Origami Nanoruler Distance Measurements. We designed and assembled DNA-origami nanorulers based on a previously described protocol (50). The assembly, purification, and flow-cell preparation of DNA-origami nanorulers is described in detail in *SI Appendix, Supplementary Information Methods*.

Microscope Setup. The microscope setup is based on a setup described in ref. 36 and described in detail in *SI Appendix, Supplementary Information Methods*.

Single-Molecule Total Internal Reflection Fluorescence (TIRF) Microscopy Data Collection. For data collection of dynein stepping, we prepared one chamber with TetraSpeck beads and another chamber on the same microscopy slide with three-color dynein either moving along microtubules or axonemes. Every data collection cycle was started by imaging a 20 × 20 grid of TetraSpeck beads. Afterward we moved to the chamber with the three-color dynein and acquired six 500-frame-long movies with 110-ms exposure times (also see *SI Appendix, Fig. S3*). After collecting the dynein movies, we moved back to the TetraSpeck beads chamber to collect another 20 × 20 grid, which was used as a control to test whether any changes in image registration occurred during acquisition (see *SI Appendix, Fig. S1*). We only accepted datasets if $\sigma_{reg} < 1$ nm. A more detailed description of the TIRF data collection is given in *SI Appendix, Supplementary Information Methods*.

Velocity and Processivity Analysis. Data for three-color-labeled dynein and GFP-tagged wild-type dynein (*SI Appendix, Fig. S2*) was acquired using μManager (51) 2.0. Subsequently, the data were analyzed in ImageJ (52) by generating kymographs and then measuring displacement as a function of time.

Bleaching Analysis of Three-Color Dynein. Data for three-color dynein labeled with either FluoroCubes (35) or conventional single dyes (*SI Appendix, Fig. S2*) was acquired using μManager (51) 2.0. Subsequently, single molecules were localized using the Spot Intensity Analysis plugin in ImageJ (52) (https://imagej.net/plugins/spot-intensity-analysis) with the following settings: time interval of 3.1 s, electron per ADU of 1.84, spot radius of 3, noise tolerance of 100 for the FluoroCube data and of 50 for the conventional dye data, and a median background estimation. The number of frames to check was set to 20 for the FluoroCube data and 10 for the conventional dye data. Afterward the data were plotted using a custom Python script as previously described (35).

Single-Molecule TIRF Data Analysis of Dynein Stepping. For the three-color dynein stepping analysis, the emitters of dynein and TetraSpeck beads were fitted and localized using the μManager (51) "Localization Microscopy' plug-in (*SI Appendix, Table S2*). After localizing all probes, we registered the three channels using the same affine-based approach as previously described for two colors (36) (*SI Appendix, Fig. S2*). Then, tracks of individual motors were extracted using the μManagers (51) "Localization Microscopy' plug-in. Afterwards a custom MATLAB (MATLAB R2019b) script to identify individual steps was applied and the data were further analyzed in a custom Python script. A detailed description of the data analysis can be found in *SI Appendix, Supplementary Information Methods*.

Image Registration and Distance Measurements for DNA-Origami Nanoruler. Image registration and distance measurements between multiple dyes on the DNA-origami nanoruler (*SI Appendix, Fig. S1*) were carried out as previously described (36). Since this is a three-color dataset instead of a two-color dataset, we carried out the distance measurements for individual spot pairs (e.g., Cy3 and ATTO 488 or Cy3 and ATTO 647N or ATTO 488 and ATTO 647N). To localize individual spots (*SI Appendix, Table S2*) and to extract spots which contained a nanoruler with all three labels, we used the μManager (51) "Localization Microscopy' plug-in. To this end, we set the minimum frame number to 18, the maximum number of missing frames to 2, the maximum distance between frames to 15 nm, the total minimum distances of the full track to 0 nm, and the maximum distances between each dye pair to 90 nm.

Negative-Stain Electron Microscopy Data Collection of Three-Color Nanoruler. For negative-stain electron microscopy, agarose gel-purified nanorulers were incubated on freshly glow-discharged carbon-coated 400 mesh copper grids for 1 min. Afterward the sample was blotted off and a 0.75% uranyl formate solution was applied immediately for staining and blotted off without incubation. This staining was repeated four times and followed by a last incubation for which the stain was incubated for 45 s before blotting. Samples were air-dried before imaging. The data were collected at the University of California, San Francisco on a Tecnai T12 microscope operating at 120 kV, using a 4,000 × 4,000 charge-coupled device camera (UltraScan 4000; Gatan).

Monte Carlo Simulation of Dynein Stepping. For the Monte Carlo simulation we used our experimental data as input. We defined a start condition (position of both MTBDs), followed by a loop of simulations for continuous stepping which ended as soon as dynein reached the minus end of the microtubule lattice. A detailed description of the conditions for the stepping loop and of the entire Monte Carlo simulation can be found in the custom Python script (https://doi.org/10.5281/zenodo.4321958) (53) and *SI Appendix, Supplementary Information Methods*.

Statistics. We discussed the inherent uncertainty due to random or systematic errors for each result and their validation in the relevant sections of the article. Moreover, we included details about sample size, number of independent calculations, and the calculation of the error bars in the figures or in the respective figure captions.

Data Availability. Raw datasets of three-color dynein stepping used in this study are hosted on Zenodo at https://doi.org/10.5281/zenodo.4321962 (54). All input datasets used for the Monte Carlo simulation of dynein stepping are hosted on Zenodo at https://doi.org/10.5281/zenodo.4321958 (53). The µManager acquisition and analysis software is available partly under the Berkeley Software Distribution (BSD) license, partly under the GNU Lesser General Public License (LGPL), and development is hosted on GitHub at https://github.com/nicost/micro-manager. The latest version for MacOS and Windows can be downloaded here: https://micro-manager.org/Download_Micro-Manager_Latest_

Release (version 2.0 gamma). A Beanshell script to run the three-color acquisition of dynein stepping is hosted on Zenodo at https://doi.org/10.5281/zenodo.4321978 (55). The custom-written Python code used to analyze three-color stepping of dynein is hosted on Zenodo at https://doi.org/10.5281/zenodo.4321962. The Python code for the Monte Carlo simulation of dynein stepping is hosted on Zenodo at https://doi.org/10.5281/zenodo.4321958. All other code is available from the authors upon request.

1. G. Bhabha, G. T. Johnson, C. M. Schroeder, R. D. Vale, How dynein moves along microtubules. *Trends Biochem. Sci.* **41**, 94–105 (2016).
2. S. Can, S. Lacey, M. Gur, A. P. Carter, A. Yildiz, Directionality of dynein is controlled by the angle and length of its stalk. *Nature* **566**, 407–410 (2019).
3. T. Kiyomitsu, I. M. Cheeseman, Cortical dynein and asymmetric membrane elongation coordinately position the spindle in anaphase. *Cell* **154**, 391–402 (2013).
4. S. L. Reck-Peterson, W. B. Redwine, R. D. Vale, A. P. Carter, The cytoplasmic dynein transport machinery and its many cargoes. *Nat. Rev. Mol. Cell Biol.* **19**, 382–398 (2018).
5. R. Viswanadha, W. S. Sale, M. E. Porter, Ciliary motility: Regulation of axonemal dynein motors. *Cold Spring Harb. Perspect. Biol.* **9**, a018325 (2017).
6. M. Taschner, E. Lorentzen, The intraflagellar transport machinery. *Cold Spring Harb. Perspect. Biol.* **8**, a028092 (2016).
7. A. J. Roberts, T. Kon, P. J. Knight, K. Sutoh, S. A. Burgess, Functions and mechanics of dynein motor proteins. *Nat. Rev. Mol. Cell Biol.* **14**, 713–726 (2013).
8. S. M. King, *Dyneins: Dynein Mechanics, Dysfunction, and Disease* (Academic Press, 2017).
9. Y. Tanaka, N. Hirokawa, "Kinesin superfamily proteins (KIFs) as a fundamental component of life: Intracellular transport and beyond" in *Encyclopedia of Cell Biology*, R. A. Bradshaw, P. D. Stahl, Eds. (Academic Press, 2016), pp. 608–619.
10. A. Gennerich, R. D. Vale, Walking the walk: How kinesin and dynein coordinate their steps. *Curr. Opin. Cell Biol.* **21**, 59–67 (2009).
11. M. A. Hartman, J. A. Spudich, The myosin superfamily at a glance. *J. Cell Sci.* **125**, 1627–1632 (2012).
12. H. L. Sweeney, A. Houdusse, Structural and functional insights into the myosin motor mechanism. *Annu. Rev. Biophys.* **39**, 539–557 (2010).
13. J. R. Kardon, R. D. Vale, Regulators of the cytoplasmic dynein motor. *Nat. Rev. Mol. Cell Biol.* **10**, 854–865 (2009).
14. M. A. Cianfrocco, M. E. DeSantis, A. E. Leschziner, S. L. Reck-Peterson, Mechanism and regulation of cytoplasmic dynein. *Annu. Rev. Cell Dev. Biol.* **31**, 83–108 (2015).
15. S. L. Reck-Peterson et al., Single-molecule analysis of dynein processivity and stepping behavior. *Cell* **126**, 335–348 (2006).
16. S. A. Burgess, M. L. Walker, H. Sakakibara, P. J. Knight, K. Oiwa, Dynein structure and power stroke. *Nature* **421**, 715–718 (2003).
17. T. Kon et al., The 2.8 Å crystal structure of the dynein motor domain. *Nature* **484**, 345–350 (2012).
18. C. Cho, S. L. Reck-Peterson, R. D. Vale, Regulatory ATPase sites of cytoplasmic dynein affect processivity and force generation. *J. Biol. Chem.* **283**, 25839–25845 (2008).
19. T. Kon, M. Nishiura, R. Ohkura, Y. Y. Toyoshima, K. Sutoh, Distinct functions of nucleotide-binding/hydrolysis sites in the four AAA modules of cytoplasmic dynein. *Biochemistry* **43**, 11266–11274 (2004).
20. T. Kon et al., Helix sliding in the stalk coiled coil of dynein couples ATPase and microtubule binding. *Nat. Struct. Mol. Biol.* **16**, 325–333 (2009).
21. L. Rao, F. Berger, M. P. Nicholas, A. Gennerich, Molecular mechanism of cytoplasmic dynein tension sensing. *Nat. Commun.* **10**, 3332 (2019).
22. I. R. Gibbons et al., The affinity of the dynein microtubule-binding domain is modulated by the conformation of its coiled-coil stalk. *J. Biol. Chem.* **280**, 23960–23965 (2005).
23. J. Lin, K. Okada, M. Raytchev, M. C. Smith, D. Nicastro, Structural mechanism of the dynein power stroke. *Nat. Cell Biol.* **16**, 479–485 (2014).
24. A. J. Roberts et al., AAA+ ring and linker swing mechanism in the dynein motor. *Cell* **136**, 485–495 (2009).
25. H. Schmidt, R. Zalyte, L. Urnavicius, A. P. Carter, Structure of human cytoplasmic dynein-2 primed for its power stroke. *Nature* **518**, 435–438 (2015).
26. G. Bhabha et al., Allosteric communication in the dynein motor domain. *Cell* **159**, 857–868 (2014).
27. M. A. DeWitt, C. A. Cypranowska, F. B. Cleary, V. Belyy, A. Yildiz, The AAA3 domain of cytoplasmic dynein acts as a switch to facilitate microtubule release. *Nat. Struct. Mol. Biol.* **22**, 73–80 (2015).
28. A. Yildiz, M. Tomishige, R. D. Vale, P. R. Selvin, Kinesin walks hand-over-hand. *Science* **303**, 676–678 (2004).
29. W. Qiu et al., Dynein achieves processive motion using both stochastic and coordinated stepping. *Nat. Struct. Mol. Biol.* **19**, 193–200 (2012).
30. M. A. DeWitt, A. Y. Chang, P. A. Combs, A. Yildiz, Cytoplasmic dynein moves through uncoordinated stepping of the AAA+ ring domains. *Science* **335**, 221–225 (2012).
31. A. Yildiz et al., Myosin V walks hand-over-hand: Single fluorophore imaging with 1.5-nm localization. *Science* **300**, 2061–2065 (2003).
32. F. B. Cleary et al., Tension on the linker gates the ATP-dependent release of dynein from microtubules. *Nat. Commun.* **5**, 4587 (2014).
33. L. G. Lippert et al., Angular measurements of the dynein ring reveal a stepping mechanism dependent on a flexible stalk. *Proc. Natl. Acad. Sci. U.S.A.* **114**, E4564–E4573 (2017).
34. H. Imai et al., Direct observation shows superposition and large scale flexibility within cytoplasmic dynein motors moving along microtubules. *Nat. Commun.* **6**, 8179 (2015).
35. S. Niekamp, N. Stuurman, R. D. Vale, A 6-nm ultra-photostable DNA FluoroCube for fluorescence imaging. *Nat. Methods* **17**, 437–441 (2020).
36. S. Niekamp et al., Nanometer-accuracy distance measurements between fluorophores at the single-molecule level. *Proc. Natl. Acad. Sci. U.S.A.* **116**, 4275–4284 (2019).
37. S. Beater, M. Raab, P. Tinnefeld, Toward quantitative fluorescence microscopy with DNA origami nanorulers. *Methods Cell Biol.* **123**, 449–466 (2014).
38. J. J. Schmied et al., Fluorescence and super-resolution standards based on DNA origami. *Nat. Methods* **9**, 1133–1134 (2012).
39. A. Keppler et al., A general method for the covalent labeling of fusion proteins with small molecules in vivo. *Nat. Biotechnol.* **21**, 86–89 (2003).
40. G. V. Los et al., HaloTag: A novel protein labeling technology for cell imaging and protein analysis. *ACS Chem. Biol.* **3**, 373–382 (2008).
41. J. Yin et al., Genetically encoded short peptide tag for versatile protein labeling by Sfp phosphopantetheinyl transferase. *Proc. Natl. Acad. Sci. U.S.A.* **102**, 15815–15820 (2005).
42. D. A. Grotjahn et al., Cryo-electron tomography reveals that dynactin recruits a team of dyneins for processive motility. *Nat. Struct. Mol. Biol.* **25**, 203–207 (2018).
43. A. Šarlah, A. Vilfan, The winch model can explain both coordinated and uncoordinated stepping of cytoplasmic dynein. *Biophys. J.* **107**, 662–671 (2014).
44. S. Ray, E. Meyhöfer, R. A. Milligan, J. Howard, Kinesin follows the microtubule's protofilament axis. *J. Cell Biol.* **121**, 1083–1093 (1993).
45. W. O. Hancock, Bidirectional cargo transport: Moving beyond tug of war. *Nat. Rev. Mol. Cell Biol.* **15**, 615–628 (2014).
46. L. S. Ferro, S. Can, M. A. Turner, M. M. ElShenawy, A. Yildiz, Kinesin and dynein use distinct mechanisms to bypass obstacles. *eLife* **8**, e48629 (2019).
47. R. Roy, S. Hohng, T. Ha, A practical guide to single-molecule FRET. *Nat. Methods* **5**, 507–516 (2008).
48. R. J. McKenney, W. Huynh, M. E. Tanenbaum, G. Bhabha, R. D. Vale, Activation of cytoplasmic dynein motility by dynactin-cargo adapter complexes. *Science* **345**, 337–341 (2014).
49. A. Yildiz, R. D. Vale, Tracking movements of the microtubule motors kinesin and dynein using total internal reflection fluorescence microscopy. *Cold Spring Harb. Protoc.* **2015**, db.prot086355 (2015).
50. J. J. Schmied et al., DNA origami-based standards for quantitative fluorescence microscopy. *Nat. Protoc.* **9**, 1367–1391 (2014).
51. A. Edelstein, N. Amodaj, K. Hoover, R. Vale, N. Stuurman, Computer control of microscopes using µManager. *Curr. Protoc. Mol. Biol.* **Chapter 14**, Unit 14.20 (2010).
52. C. A. Schneider, W. S. Rasband, K. W. Eliceiri, NIH Image to ImageJ: 25 years of image analysis. *Nat. Methods* **9**, 671–675 (2012).
53. S. Niekamp, N. Stuurman, N. Zhang, R. D. Vale, Code from "Python code for Monte Carlo Simulation of dynein stepping." *Zenodo*. https://doi.org/10.5281/zenodo.4321958. Deposited 15 December 2020.
54. S. Niekamp, N. Stuurman, N. Zhang, R. D. Vale, Code and data from "Python code and experimental data of three-color dynein stepping." *Zenodo*. https://doi.org/10.5281/zenodo.4321962. Deposited 15 December 2020.
55. S. Niekamp, N. Stuurman, N. Zhang, R. D. Vale, Code from "Acquisition code to collect three-color stepping data of dynein." *Zenodo*. https://doi.org/10.5281/zenodo.4321978. Deposited 15 December 2020.
56. N. Nishida et al., Structural basis for two-way communication between dynein and microtubules. *Nat. Commun.* **11**, 1038 (2020).

BIOPHYSICS AND COMPUTATIONAL BIOLOGY